Journal of Materials Chemistry A

Accepted Manuscript

This article can be cited before page numbers have been issued, to do this please use: A. R. Uhl, Z. Yang, A. Jen and H. Hillhouse, *J. Mater. Chem. A*, 2017, DOI: 10.1039/C7TA00562H.

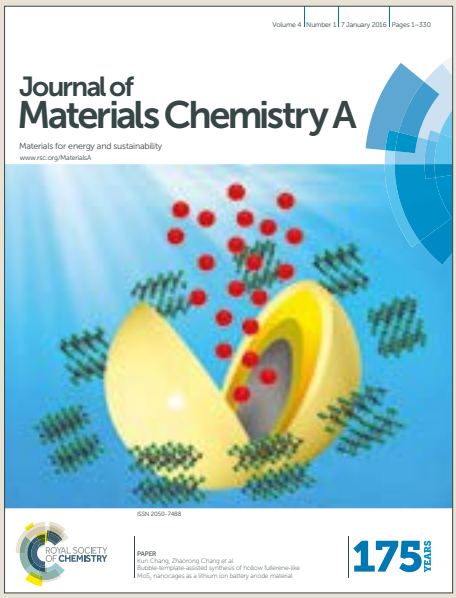

ROYAL SOCIETY OF CHEMISTRY

rsc.li/materials-a

Journal of Materials Chemistry A

COMMUNICATION

Solution-processed chalcopyrite-perovskite tandem solar cells in bandgap-matched two- and four-terminal architectures

Alexander R. Uhl,[‡*a] Zhibin Yang,[‡b] Alex K.-Y. Jen,[*b] Hugh W. Hillhouse*[a]

Received 17th January 2017,
Accepted 27th January 2017

DOI: 10.1039/C7TA00562H

www.rsc.org/

Solution-processed chalcopyrite and perovskite devices of various bandgaps are combined in four- and two-terminal mechanically stacked tandem architectures. The excellent low-light performance of Cu(In,Ga)(S,Se)$_2$ and low-bandgap CuIn(S,Se)$_2$ cells and the high efficiency of novel NIR-transparent inverted perovskite cells with C_{60}/bis-C_{60}/ITO as electron transport layers, enabled stabilized two- and four- terminal tandem efficiencies up to 18.5% and 18.8%, respectively, which represents a new record for tandem devices with solution-processed chalcopyrite and perovskite absorbers.

Tandem solar cells present an exciting means for increasing the efficiency of solar modules, thereby reducing their balance of system cost (BOS) and potentially the cost per watt peak ($/Wp) of a module. A conventional tandem solar cell is fabricated such that a pn junction that employs a large bandgap absorber is above of a pn junction that employs a small bandgap absorber in order to improve the utilization of the solar spectrum and reduce the thermalization losses of photons.[1,2] Under one Sun irradiation, the theoretical maximum efficiency can be increased from 30% up to 42% from a single to a double junction.[3] Highest efficiency tandem solar cells are typically based on III-V semiconductors and have achieved up to 31.1% efficiency under one Sun.[4] However, the high material cost and expensive epitaxial layer growth of III-V semiconductors limit tandem devices to special markets such as concentrator photovoltaics or extra-terrestrial applications.

Tandem solar cells composed of Cu(In,Ga)(S,Se)$_2$ (CIGS), CuIn(S,Se)$_2$ (CIS) and hybrid-perovskite (HP) thin film solar cells could dramatically reduce the cost and approach electricity prices as low as those from coal and natural gas.[5-8] Both technologies have achieved power conversion efficiencies (PCEs) of over 20% with bandgaps that are just short of the theoretical maximum at 1.4 eV, i.e. 1.62 eV for HP and 1.15 eV for CIGS.[9,10] The combination of both absorber types in a tandem device, however, could turn this shortcoming into an advantage. Simulations predict optimum bandgaps of 1.6 - 1.9 eV for top cells and 0.9 - 1.2 eV for bottom cells, which are accessible for HP and CIGS cells by changing the Br/(Br+I) and Ga/(Ga+In) and S/(S+Se) ratios, respectively.[3,11,12] A further advantage of both technologies is the possibility of solution processing which provides the potential for highly reduced manufacturing cost. The thin film nature of both cells allows for

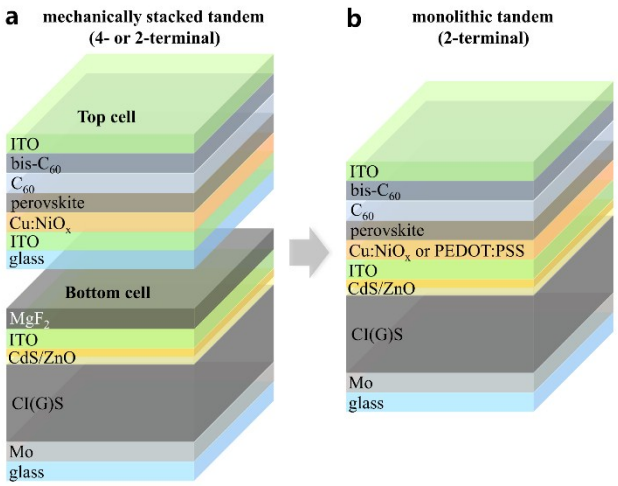

Fig. 1: Schematic of a mechanically stacked (a) and a monolithic tandem device (b). The large bandgap, semi-transparent perovskite top cell is placed (a) or deposited (b) on top of a low-bandgap Cu(In,Ga)(S,Se)$_2$ or CuIn(S,Se)$_2$ bottom cell. The mechanically stacked architecture (used in this study) allows for operation in either four-terminal or two-terminal (i.e. current-matched) configuration while the monolithic architecture is two-terminal only. The energy level diagram of the perovskite top cell is depicted in Fig. S1.

[a] *Department of Chemical Engineering, University of Washington, Seattle, WA 98195, USA. Email: auhl@uw.edu; h2@uw.edu.*
[b] *Department of Materials Science and Engineering, University of Washington, Seattle, WA 98195, USA. Email: ajen@uw.edu.*
[‡] *These authors contributed equally to this work.*
Electronic Supplementary Information (ESI) available: Experimental details, optical spectra of filters and devices, detailed performance data, ICP-MS, and XRD. See DOI: 10.1039/x0xx00000x

monolithic integration and a wide choice of rigid or flexible substrates which could further reduce cost by enabling the possibility for high-throughput roll-to-roll processing.[13-15]

Tandem solar cells can be fabricated by either mechanically stacking cells or fabricating top cells directly on the bottom cell (see Fig. 1). Mechanically stacked devices (used in this study) are typically easier to fabricate in the lab as they allow independent processing of top and bottom cells and both parallel (four-terminal) or series connection (two-terminal) between the cells. In contrast, monolithically grown tandem cells are inherently connected in series and always require current matching between the top and bottom cell. Process parameters and treatments of all consecutive layers need to be appropriately selected to be consistent with all previously deposited layers. These drawbacks, however, are offset by the cost savings in manufacturing (i.e. monolithic integration and omission of an additional substrate and electrode) and improved performance from reduced optical and resistive losses, making monolithic two-terminal tandem devices the economically advantageous choice.[8,16,17]

Hybrid perovskites are ideally suited as top cells in tandem devices as they exhibit low sub-bandgap absorption and can be deposited at low temperatures, which is indispensable to avoid degradation of the CIGS bottom cell during processing.[18-20] Device efficiencies up to 15.9% have been reported for HP devices with all employed processing temperatures below 150°C.[21] All layer solution-processed HP solar cells using temperatures below 120°C resulted in up to 11.5% PCE.[15] Theoretical bandgaps for perovskites range from 1.57 - 2.29 eV for $MAPbX_3$ ($X = Cl^-, Br^-, I^-$) and 1.48 - 2.23 eV for $FAPbX_3$ absorber compounds, with larger bandgaps and improved morphology for increased Br and Cl content, respectively. While the perovskite bandgap is tunable over a wide range, highest device efficiencies have been obtained for bandgaps between 1.5 - 1.6 eV,[10,22-25] which is an excellent fit with 1.0 eV bandgap $CuInSe_2$ bottom cells in current-matched monolithic tandem devices.[1,3,11,12,26] Furthermore, recent studies suggest that improved material properties and device stability could limit perovskites to intermediate bandgap compositions around 1.6 eV with low bromide content or tri-cation compositions with Cs, formamidinium (FA), and methylammonium (MA),[10,27,28] which further amplifies the need for combination with low bandgap bottom cells. An additional requirement for HP cells in the tandem configuration is the replacement of opaque layers like metal contacts with transparent layers to allow NIR light transmission to the bottom cell. Promising results have already been obtained with MoO_3/ITO, nanoparticles/ITO, MoO_3/Al:ZnO, Ag nanowires, or thin metal layers.[16,17,29-32]

Several tandem devices with HP top cells and Si bottom cells have been reported to date with PCEs up to 25.2% for four-terminal and 21.2% for monolithic devices.[32-34] But while these efficiencies are very exciting, the use of silicon for the bottom cell imposes restrictions due to silicon's relatively high bandgap of 1.14 eV, limitation to rigid substrates due to the use of monocrystalline Si wafers, and high fabrication cost of the latter. Recently, solution-processed HP/HP tandems have been reported with notable efficiencies up to 20.3% and 17.0% for four-terminal and two-terminal tandems, respectively.[35] However, the large bandgap of the Sn-based bottom cell absorber of 1.2 eV might limit further improvements for current-matched devices. Tandem solar cells with HP top cells and co-evaporated CIGS bottom cells have achieved up to 20.5% for four-terminal devices.[29,36] Using solution deposited CIGS absorbers from hydrazine inks, Yang et al. and Todorov et al. presented four-terminal tandem devices up to 15.5% efficiency and two-terminal devices up to 15.9% for mechanically stacked and 10.9% efficiency for monolithic tandem devices, respectively.[37,38] While these values are noteworthy, tandem devices were limited by low transmission or high resistance of the employed electrodes or reduced efficiencies of the small bandgap bottom cells.

Here, we present new record efficiencies for bandgap-matched tandem devices with solution-processed perovskite and chalcogenide absorbers. The bottom cells are low-bandgap CIGS (1.0 to 1.2 eV) formed from molecular-inks with non-toxic solvent dimethyl sulfoxide (DMSO).[39] The top cells are optically NIR-transparent solution-processed lead halide based perovskite cells with bandgaps from 1.5 - 1.7 eV.[40] We show device results for mechanically-stacked two- and four-terminal configurations with stabilized AM1.5 power conversion efficiencies of up to 18.5% and 18.8%, respectively. For the two-terminal case, we find that optimal current matching is obtained for devices with 1.5 - 1.6 eV and 1.0 eV bandgap. Further, we present exceptional low-light performance from the solution-processed chalcogenide cells with stable or increasing fill factor and efficiency at reduced light intensity and with UV- and visible- filtered light (NIR only). The low-light performance of the bottom cell, the novel semi-transparent architecture of the top cell, and the improved conversion efficiencies of the combined tandem devices, highlight the potential of solution-processed perovskite and chalcogenide tandem cells.

In order to fabricate efficient tandem devices, a number of topics have to be considered such as the high transparency of the top cell, current matching in two-terminal devices, and adequate processing parameters of top layers during monolithic fabrication. An additional area, that is often overlooked, is the low light performance of the bottom cells. As light is passing through the top cell, both the total irradiance as well as the UV and visible portion of the AM1.5G spectrum is reduced for the bottom cell. Typically, this has a negative influence on the performance due to the logarithmic dependence of Voc with irradiance and the increasing influence of the shunt resistance at low light intensities.[41] The performance of Si and CIGS solar cells at 10% irradiance has been reported to decrease by 10% and 20%, respectively.[41,42] This is a significant problem, considering that typical semi-transparent perovskite top cells allow a total transmission of around 30-50% of the solar spectrum to the bottom cell (see Fig. S2).

To investigate the low light performance of our solution-processed $Cu(In,Ga)(S,Se)_2$ and $CuIn(S,Se)_2$ cells we measured their J(V) characteristics under AM1.5G light with various applied filters. Neutral density filters were varied from optical density (OD) 0, 0.1, 0.5, to 1 while a selection of consecutive long-pass (LP) filters was applied to achieve effective cut-off wavelengths at 440 nm, 530 nm,

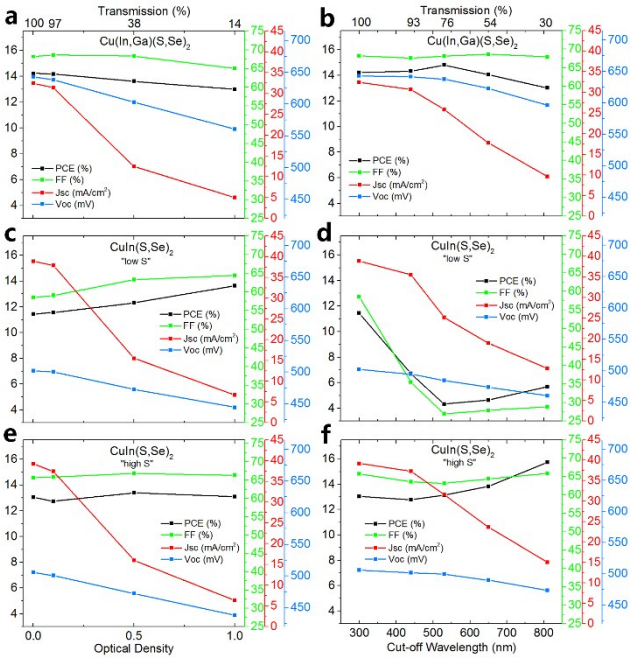

Fig. 2: Low-light performance of CIGS (a, c) and CIS devices with low S (c, d) and high S content (e, f). The lack of the UV- and visible portion of the light leads to a pronounced FF loss in case of the Ga-free samples with low S content. Neutral density filters of OD 0.1, 0.5, and 1 (left column) and long pass filters of 440 nm, 530 nm, 650 nm, and 810 nm (right column) were employed to reduce the irradiance (See SI for transmission data of filters). OD 0 and cut-off at 300 nm correspond to unfiltered light. The transmission values of the used filters and respective cell performance was estimated from the current of a Si diode.

650 nm, and 810 nm (see Fig. S3). The corresponding transmission values of the respective filters were estimated from the short circuit current of a Si diode. The results are summarized in Figure 2. As expected, the Voc of both CIGS and CIS follows a linear trend with the optical density of the neutral density filters, being the negative decadic logarithm of the transmission. The current density decreases exponentially with optical density and linearly with transmission. The FF for CIGS cells exhibits a slight increase at OD 0.1 but then overall decrease from 69% to 65% with lower transmission, which is in agreement to previous reports.[42] In contrast, CIS cells (Fig. 2c, d) show a steady increase in FF from 59% to 65% from OD 0 to OD 1. A closer look at the resistances (see Table S1) shows that this behavior is due to a four to three-fold increase in series resistance that is overcompensated, in the case of CIS, by a doubling and sextupling shunt resistance for CIGS and CIS, respectively. Overall, this leads to a slightly decreasing efficiency for CIGS (14.2% to 13.0%) and increasing efficiency for CIS solar cells with reduced irradiance (11.4% to 13.6%). The behavior, however, is vastly different for spectrally filtered light (see Fig. 2d and Fig. S4). Similar to the OD filters, Voc and Jsc decreases with decreasing transmission. But while the FF for CIGS is fairly stable at 68%, it drops sharply to less than half of its value from 58% to 27% for CIS cells. The lowest fill factor is seen at a cut-off wavelength of 530 nm, which is just slightly below the bandgap of CdS, i.e. 2.4 eV. For cut-off wavelengths above this value, the FF increases again following the trend from reduced irradiance with OD filters. The efficiency follows this change and drops from 11.4% down to 4.3% at 530 nm cut-off wavelength.

This drop in fill-factor may be explained by considering: (1) the barrier height for photo-generated electrons in the absorber layer to cross over into the buffer layer, commonly referred to as a positive conduction band offset or "spike," [43,44] and (2) the kinetic energy that the photo-generated electrons have as a result of acceleration from the built-in electric field in the absorber. Any increase in the height of the barrier or decrease in the electron kinetic energy due to a decrease in band bending may cause a serious loss in fill factor. The barrier height in the conduction band going from a $Cu(In,Ga)(S,Se)_2$ material to CdS is largest for gallium- and sulfur-free $CuInSe_2$ due to its lower conduction band. This makes the transmission rate of the photo-generated electron over the barrier especially sensitive to the band bending. It is also well known that due to the trapping and de-trapping dynamics from defects in CdS high energy photons (2.4 eV and higher) shift the Fermi-level in CdS higher and thus increase the band bending in the absorber layer.[44,45] Under normal full-spectrum illumination this upward shift in the Fermi-level in the CdS (and increased band bending in the absorber) is typically enough to allow photo-generated electrons to cross the barrier. However, since the high energy portion of the light up to 800 nm – for a $FAPbI_3$ perovskite – will be absorbed by the top cell, this is problematic for some CIS cells in tandem devices. However, not all of our CIS cells exhibited this sort of behavior. We noticed that certain CIS cells showed no significant changes in FF under UV and visible filtered light (see Fig. 2 e, f and Table S2) and in fact displayed improved efficiencies from 13% to 16% when the high energy portion up to 810 nm was filtered out. The champion CIS cell, that we also used for the remaining part of this paper and that even exceeded PCEs of our CIGS cells at lowest filtered light conditions, exhibited a slightly altered composition with a higher sulfur to selenium ratio (i.e. 0.06 instead of 0.01, see Table S3) and the corresponding peak shifts in X-ray diffraction towards higher diffraction angles (see Fig. S5). It showed 30% lower series and 5% higher shunt resistance while the diode ideality factor was reduced from 2.5 to 1.85, as compared to the "low S" cell in Fig. 2 c, d. This suggests that the improved performance of the champion CIS device is due to a reduction of the barrier in the conduction band by an increase in sulfur. In contrast to CIGS absorbers, where the sulfur addition mainly affects the valence band, small amounts of sulfur are reported to lift the conduction band in Ga-free CIS absorbers, thereby reducing the spike towards the buffer.[46] This is consistent with the observed reduction in diode ideality factor which suggests a transition from dominant recombination in the space-charge region (potentially tunneling enhanced) where the electron and hole populations are nearly equal, to an increasing contribution from recombination in the quasi-neutral region where electron and hole populations are vastly different and typically result in lower overall recombination.[47]

While we only report on mechanically stacked tandem cells in this paper, we designed the device architecture in such a way that it allows for the implementation in monolithic devices. Perovskite cells

are typically fabricated in the p-i-n heterojunction configuration with the perovskite being sandwiched between a p-type hole transport layer (HTL) and n-type electron transport layer (ETL). Processing temperatures of charge transporting layers and device integration determine the use of either conventional architecture (substrate/cathode/ETL/HP/HTL/anode) or inverted structure (substrate/anode/HTL/HP/ETL/cathode).[48] Highest efficiency devices to date, of up to 21.1% PCE, have been obtained in the conventional configuration with TiO_2 as the ETL and PTAA or spiro-OMeTAD as the HTL.[10,22,25,49] However, this electrode polarity is not suited for monolithic processing on typical chalcogenide cells in substrate configuration with a metal anode and a TCO cathode (see Fig. 1). Moreover, TiO_2 blocking or mesoporous layers typically require high temperature calcination steps between 450-550°C for 30-60 min,[22,29,49] which is incompatible with CIGS solar cells. Devices with inverted architecture employing mostly C_{60} as the ETL have yielded up to 15.4% PCE.[50] Bis-C_{60} surfactant is thereby used to ensure benign band alignment between C_{60} and the metal cathode.[51] In a tandem device, however, the substitution of metal layers by transparent electrodes is required to allow light transmission to the bottom cell. Promising results have already been obtained with Ag nanowires or thin metal layers but high transmission and conductivities can typically not be obtained at the same time.[16,29] Noteworthy results with ITO top electrodes were reported by Bush et al. and McMeekin et al. with stabilized PCEs up to 12.3% and 12.5% when ITO was sputtered on a nanoparticle buffer layer to reduce the sputter impact.[31,32]. ITO is a highly attractive and commonly used material due to its very high conductivity, high transparency, and appropriate work function.[48,52] In this work, we deposited a ITO cathode directly on a bis-C_{60}/C_{60} double layer. The bis-C_{60} surfactant layer was added between ITO and C_{60} to aid the band alignment (see Fig. S1), while the problem of sputter damage was mitigated by employing a "soft" sputter process at low power of 150 W and pressures under 3 mTorr of Ar. ITO is also less sensitive to degradation in moisture and was seen to prolong the lifetime of our HP devices. Copper doped NiO_x was used as HTL in our device structure in combination with ITO to fabricate NIR-transparent devices (see Fig. 3a). Compared to PEDOT:PSS, Cu:NiO_x has advantages of having a lower valence band maximum and higher air stability and can be deposited at low temperatures around 150°C using the reported combustion method.[53,54]

To investigate the optimum utilization of the solar spectrum in a two junction tandem device, we fabricated semi-transparent perovskite devices with three different bandgaps of 1.51 eV, 1.59 eV, and 1.70 eV to combine them with our chalcogenide cells of bandgap 0.99 eV and 1.15 eV (Fig. 3b, S6). From the original $MAPbI_3$ structure the bandgap was widened to 1.70 eV by partial substitution of I^- with Br^- while the bandgap was decreased by replacing the organic cation MA with FA.[40] Devices were fabricated by applying the ITO cathodes through a shadow mask with 10 mm^2 aperture area while mirror samples with similar transmission (see Fig. S2) with unmasked ITO were used for the tandem experiments. To project the performance of both two- and four terminal tandem devices we measured the J(V) characteristic of CIS and CIGS cells with various perovskite filters

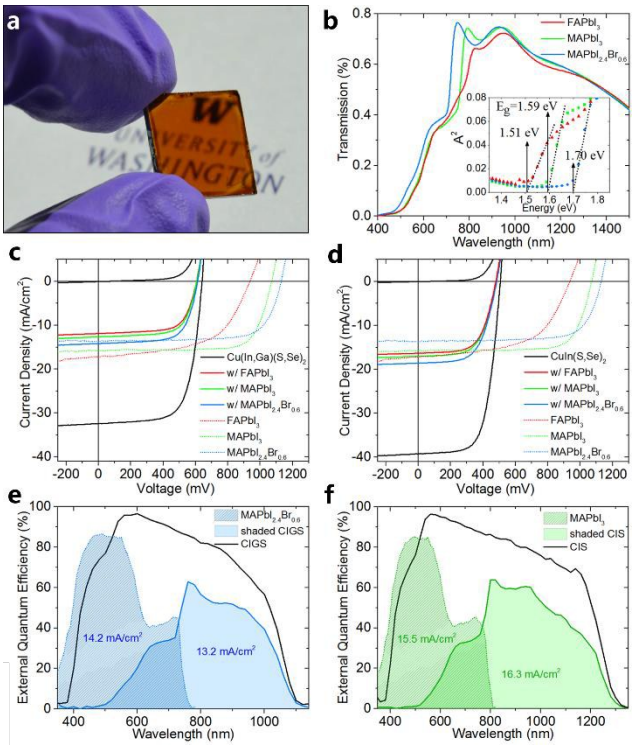

Fig. 3: (a) Photograph of a semi-transparent perovskite solar cell. (b) Transmission and squared absorbance of perovskite filters used in table 1. The bandgaps are extracted to 1.51 eV, 1.59 eV, and 1.70 eV for $FAPbI_3$, $MAPbI_3$, and $MAPbI_{2.4}Br_{0.6}$ respectively. (c-d) J(V) measurements of perovskite cells, CI(G)S devices, and CI(G)S devices with perovskite filters. (e-f) External quantum efficiency data of perovskites and shaded chalcogenide cells that yielded highest two-terminal tandem PCEs in this paper (projected PCE). Excellent current matching is obtained for $Cu(In,Ga)(S,Se)_2$ and $MAPbI_{2.4}Br_{0.6}$ as well as for $CuIn(S,Se)_2$ and $MAPbI_3$, and $CuIn(S,Se)_2$ and $FAPbI_3$, respectively.

between the AM1.5G light source and the chalcogenide device. The J(V) curves of all perovskite cells and the corresponding filtered chalcogenide devices are shown in Fig. 3c and Fig. 3d for the CIGS and CIS cells, respectively. As expected, the current densities of the filtered devices follows the increase in bandgaps from $FAPbI_3$, to $MAPbI_3$, to $MAPbI_{2.4}Br_{0.6}$. In agreement with theoretical predictions,[3,11,12] excellent current matching between the perovskite cell and the filtered chalcogenide is observed for the combinations of CIGS with $MAPbI_{2.4}Br_{0.6}$, i.e. 1.15 eV and 1.70 eV, CIS with $FAPbI_3$, i.e. 0.99 eV and 1.51 eV, and CIS with $MAPbI_3$, i.e. 0.99 eV and 1.59 eV. External quantum efficiency measurements (EQE) and calculated Jsc values from EQE for perovskite and shaded chalcogenide cells confirm this finding (Fig. 3 e-f).

The semi-transparent perovskite devices without antireflection coating exhibited PCEs up of 9.03%, 12.5%, and 11.3% for $FAPbI_3$, $MAPbI_3$, and $MAPbI_{2.4}Br_{0.6}$ with current densities of 17.2 mA/cm^2, 15.8 mA/cm^2, and 13.7 mA/cm^2 (see Table 1), that agree well with the calculated values from EQE (Fig. 3c-d, S7). The perovskite cells exhibited stable performance under illumination, and in fact improved their efficiency to 9.03%, 13.6%, and 11.8% after holding the devices at maximum power point for 600 s, which is amongst the

Table 1: Table of measured conversion efficiencies of perovskites, CI(G)S, and filtered CI(G)S cells. Both mechanically-stacked four- and two-terminal conversion efficiencies are calculated (see Fig. S8-S9). Best bandgap matching is observed for a combination of the 1.0 eV and 1.6 eV bandgap cells to yield a projected two-terminal power conversion efficiency of 17.8% (18.5% stabilized). Four-terminal efficiencies up to 17.8% (18.8% stabilized) are obtained by a combination of 1.2 eV and 1.6 eV bandgap devices.

Test condition	Egap (eV)	Voc (mV)	Jsc (mA/cm^2)	FF (%)	PCE (%)	4-term PCE (%)	2-term PCE (%)
$FAPbI_3$	1.51	940	17.2	56	9.03 (9.73*)		
$MAPbI_3$	1.59	1070	15.8	74	12.5 (13.6*)		
$MAPbI_{2.4}Br_{0.6}$	1.70	1130	13.7	73	11.3 (11.8*)		
$Cu(In,Ga)(S,Se)_2$	1.15	639	32.4	68.7	14.3		
w/ $FAPbI_3$		604	11.9	68.2	4.90$^+$	13.9 (14.6*)	12.9
w/ $MAPbI_3$		605	12.6	68.2	5.22$^+$	**17.8 (18.8*)**	15.7
w/ $MAPbI_{2.4}Br_{0.6}$		611	14.2	68.3	5.90$^+$	17.2 (17.7*)	17.2
$CuIn(S,Se)_2$	0.99	506	39.2	65.7	13.0		
w/ $FAPbI_3$		478	16.3	62.8	4.90$^+$	13.9 (14.6*)	13.9 (14.6*)
w/ $MAPbI_3$		480	17.0	62.0	5.06$^+$	17.6 (18.7*)	**17.8 (18.5*)**
w/ $MAPbI_{2.4}Br_{0.6}$		483	18.6	61.2	5.49$^+$	16.8 (17.3*)	16.1 (16.9*)

* Stabilized projected tandem efficiencies estimated from perovskites PCEs after 600 s at maximum power point (see Fig. S9).
$^+$ PCE with filters, not accounting for the reduced irradiance with filters.

highest PCEs for stabilized semi-transparent perovskite devices in inverted architecture or with sputtered ITO electrodes.[31,32,35,38] The used chalcogenide cells exhibited PCEs of 14.3% for CIGS and 13.0% for low-bandgap CIS absorbers, which is the highest reported PCE for a solution-processed solar cell with a bandgap of 1.0 eV.[39] When we measured the performance of our chalcogenide devices with the above described perovskite filters, reducing the irradiance and the UV- and visible portion of the light, the current density and efficiency (uncorrected for reduced irradiance) dropped roughly to a third due to the 31-37% total transmission of the perovskites filters. As expected from our previous experiments with ND and LP filters, the Voc decreased logarithmically with irradiance while the FF declined just marginally for these cells. By adding the efficiencies of the perovskite and filtered chalcogenide cells, four-terminal tandem efficiencies of up to 17.8% and 17.6% (18.8% and 18.7% with stabilized perovskites) were calculated for $MAPbI_3$ top and CIGS and CIS bottom cells, respectively. To our knowledge, these values represent the highest reported four-terminal tandem efficiencies with solution processed chalcogenide and perovskite absorbers, i.e. 10.8% by Lee at al. and 15.5% by Yang et al.,[37,55] and even some reports with vacuum deposited chalcogenide bottom cells, i.e. 18.6% efficiency by Bailie et al.[29] While the record four-terminal device simply follows the champion efficiencies of the individual top and shaded bottom cells, the projection of a two-terminal efficiency is a bit more complex.[56,57] The current density of the two-terminal tandem device is limited by the minimum current of the individual cells. However, the maximum power in a two-terminal devices is not necessarily at maximum current since the FF increases with increasing current mismatch.[57] Additionally, low shunt resistances of the individual cells can lead to leakage currents and further limit the current density. Considering all of the above, we projected the two-terminal performances for all chalcogenide and perovskite combinations and found the highest efficiency of 17.8% for the combination of the $MAPbI_3$ cell and the low bandgap CIS device (Table 1 and Fig. S8). It is noteworthy that for this combination, the projected two-terminal performance is even higher than for the four-terminal device, which highlights the effect of the FF improvements with current mismatch. The projected two-terminal efficiency for stabilized cells exhibits a record value of 18.5% (see Table 1 and Fig. S9), which is the highest reported value for a solution-processed two-terminal tandem device, exceeding HP/HP tandem devices of 17.0%,[35] HP/polymer tandem devices of up to 16%,[58] and HP/chalcogenide tandems up to 15.9%.[38] The excellent current matching of our solution processed low-bandgap CIS cell with our highly efficient, NIR-transparent $MAPbI_3$ perovskite cells is accountable for this high two-terminal performance that exceeds even some recent reports of two-terminal devices with 1.1 eV bandgap silicon or 1.2 eV bandgap perovskite bottom cells.[35,59]

Conclusions

Measurements of both CIS and CIGS solar cells at reduced irradiance and UV- and visible filtered light elucidate their suitability as bottom cells in tandem devices. We found excellent low-light performance for both absorber types with bandgaps of 1.15 eV and 0.99 eV. For Ga-free absorbers, however, elevated S/Se ratios around 0.06 were seen to be necessary to avoid FF and performance losses that can be as high as 50%. NIR-transparent perovskite devices with up to 13.6% stabilized efficiency (without antireflection coating) were fabricated with C_{60}/bis-C_{60}/ITO as ETL in the inverted architecture using layers that can be deposited below 150°C, allowing their use in monolithic tandem processing. Perovskite cells with bandgaps of 1.51 eV, 1.59 eV, and 1.70 eV were combined with chalcogenide bottom cells of 0.99 eV and 1.15 eV bandgap in both mechanically-stacked four- and two-terminal tandem configuration. Stabilized four-terminal efficiencies up to 18.8% were obtained by combining CIGS and $MAPbI_3$ cells in a tandem, which exhibits the highest PCE for a tandem device with solution-processed chalcogenide and perovskite absorbers exceeding even some reports with vacuum-processed CIGS bottom cells.[29] For stabilized, two-terminal tandem devices we project up to 18.5% efficiency by combining a $MAPbI_3$ top and CIS bottom cell for excellent bandgap matching. This presents the highest PCE for a two-terminal tandem with solution-processed absorbers and even some reports with Si or perovskite bottom cells, highlighting the excellent suitability of low bandgap $CuIn(S,Se)_2$ absorbers for tandems with perovskites. Further performance improvements are expected from reducing reflection, absorption, and resistive losses in our tandem devices. The application of anti-reflection coatings on each side of the perovskite device can reduce the high reflection losses (see Fig. S2) and is expected to increase the performance by more than 10%. Simulations can support the determination of optimal thicknesses of absorbers and TCOs for optimal current matching and carrier transport while the fabrication

of monolithic devices will ultimately remove losses in glass and the additional ITO layer. These encouraging tandem device results for solution-processed perovskite and chalcogenide absorbers and the thin film nature of both PV technologies might pave the road for future high-throughput, roll-to-roll printed, high efficiency monolithic tandem devices that could ultimately lead to ultra-low cost solar modules and dramatically reduce the cost of clean and sustainable electricity from the sun.

Acknowledgements

ARU acknowledges the financial support from the Swiss National Science Foundation (SNSF) under project number P2EZP2_152168 and P300P2_164660. This work was financially supported by the U.S. Department of Energy Sunshot Initiative "Next Generation Photovoltaics 3" with the award number DE-EE0006710. Part of this work was conducted at UW NNCI Washington Nanofabrication Facility at University of Washington. ZY thanks the financial support from the State of Washington through the University of Washington Clean Energy Institute.

References

1. A. Polman and H. A. Atwater, *Nature Materials*, 2012, **11**, 174-177.
2. T. Ameri, G. Dennler, C. Lungenschmied and C. J. Brabec, *Energy Environ. Sci.*, 2009, **2**, 347-363.
3. A. De Vos, *J. Phys. D: Appl. Phys.*, 1980, **13**, 839.
4. M. A. Steiner, J. F. Geisz, I. Garcia, D. J. Friedman, A. Duda, W. J. Olavarria, M. Young, D. Kuciauskas and S. R. Kurtz, *IEEE Journal of Photovoltaics*, 2013, **3**, 1437-1442.
5. M. A. Green, A. Ho-Baillie and H. J. Snaith, *Nature Photonics*, 2014, **8**, 506-514.
6. R. F. Service, *Science*, 2014, **344**, 458.
7. M. Liu, M. B. Johnston and H. J. Snaith, *Nature*, 2013, **501**, 395-398.
8. Z. M. Beiley and M. D. McGehee, *Energy Environ. Sci.*, 2012, **5**, 9173-9179.
9. P. Jackson, R. Wuerz, D. Hariskos, E. Lotter, W. Witte and M. Powalla, *physica status solidi (RRL) - Rapid Research Letters*, 2016, **10**, 583-586.
10. M. Saliba, T. Matsui, J.-Y. Seo, K. Domanski, J.-P. Correa-Baena, M. K. Nazeeruddin, S. M. Zakeeruddin, W. Tress, A. Abate, A. Hagfeldt and M. Grätzel, *Energy Environ. Sci.*, 2016, **9**, 1989-1997.
11. S. R. Kurtz, P. Faine and J. M. Olson, *J. Appl. Phys.*, 1990, **68**, 1890.
12. F. Meillaud, A. Shah, C. Droz, E. Vallat-Sauvain and C. Miazza, *Sol. Energ. Mat. Sol. C.*, 2006, **90**, 2952–2959.
13. A. Chirilă, S. Buecheler, F. Pianezzi, P. Bloesch, C. Gretener, A. R. Uhl, C. Fella, L. Kranz, J. Perrenoud, S. Seyrling, R. Verma, S. Nishiwaki, Y. E. Romanyuk, G. Bilger and A. N. Tiwari, *Nature Materials*, 2011, **10**, 857-861.
14. P. Docampo, J. M. Ball, M. Darwich, G. E. Eperon and H. J. Snaith, *Nat. Commun.*, 2013, **4**, 2761.
15. J. You, Z. Hong, Y. M. Yang, Q. Chen, M. Cai, T.-B. Song, C.-C. Chen, S. Lu, Y. Liu, H. Zhou and Y. Yang, *ACS Nano*, 2014, **8**, 1674-1680.
16. T. Todorov, T. Gershon, O. Gunawan, C. Sturdevant and S. Guha, *Appl. Phys. Lett.*, 2014, **105**, 173902.
17. P. Loper, S. Moon, S. M. deNicolas, B. Niesen, M. Ledinsky, S. Nicolay, J. Bailat, J. Yum, S. DeWolf and C. Ballif, *Phys. Chem. Chem. Phys.*, 2015, **17**, 1619-1629.
18. S. Kijima and T. Nakada, *Appl. Phys. Express*, 2008, **1**, 075002.
19. F. Johnson, S. H. Song, J. Abrahamson, R. Liptak, E. Aydil and S. A. Campbell, *Sol. Energ. Mat. Sol. C.*, 2015, **132**, 515–522.
20. S. D. Wolf, J. Holovsky, S.-J. Moon, P. Löper, B. Niesen, M. Ledinsky, F.-J. Haug, J.-H. Yum and C. Ballif, *J. Phys. Chem. Lett.*, 2014, **5**, 1035-1039.
21. K. Wojciechowski, M. Saliba, T. Leijtens, A. Abate and H. J. Snaith, *Energy Environ. Sci.*, 2014, **7**, 1142-1147.
22. W. S. Yang, J. H. Noh, N. J. Jeon, Y. C. Kim, S. Ryu, J. Seo and S. I. Seok, *Science*, 2015, **348** 1234-1237.
23. N. J. Jeon, J. H. Noh, W. S. Yang, Y. C. Kim, S. Ryu, J. Seo and S. I. Seok, *Nature*, 2015, **517**, 476-480.
24. N. J. Jeon, J. H. Noh, Y. C. Kim, W. S. Yang, S. Ryu and S. I. Seok, *Nature Materials*, 2014, **13**, 897-903.
25. H. Zhou, Q. Chen, G. Li, S. Luo, T.-b. Song, H.-S. Duan, Z. Hong, J. You, Y. Liu and Y. Yang, *Science*, 2014, **345**, 542-546.
26. J. P. Mailoa, M. Lee, I. M. Peters, T. Buonassisi, A. Panchula and D. N. Weiss, *Energy Environ. Sci.*, 2016, **9**, 2644-2653.
27. I. L. Braly and H. W. Hillhouse, *J. Phys. Chem. C*, 2016, **120**, 893-902.
28. E. T. Hoke, D. J. Slotcavage, E. R. Dohner, A. R. Bowring, H. I. Karunadasa and M. D. McGehee, *Chem. Sci.*, 2015, **6**, 613-617.
29. C. D. Bailie, M. G. Christoforo, J. P. Mailoa, A. R. Bowring, E. L. Unger, W. H. Nguyen, J. Burschka, N. Pellet, J. Z. Lee, M. Grätzel, R. Noufi, T. Buonassisi, A. Salleo and M. D. McGehee, *Energy Environ. Sci.*, 2015, **8**, 956-963.
30. L. Kranz, A. Abate, T. Feurer, F. Fu, E. Avancini, J. Löckinger, P. Reinhard, S. M. Zakeeruddin, M. Grätzel, S. Buecheler and A. N. Tiwari, *J. Phys. Chem. Lett.*, 2015, **6**, 2676-2681.
31. K. A. Bush, C. D. Bailie, Y. Chen, A. R. Bowring, W. Wang, W. Ma, T. Leijtens, F. Moghadam and M. D. Gehee, *Advanced Materials*, 2016, **28**, 3937-3943.
32. D. P. McMeekin, G. Sadoughi, W. Rehman, G. E. Eperon, M. Saliba, M. T. Hörantner, A. Haghighirad, N. Sakai, L. Korte, B. Rech, M. B. Johnston, L. M. Herz and H. J. Snaith, *Science*, 2016, **351**, 151-155.
33. J. Werner, L. Barraud, A. Walter, M. Bräuninger, F. Sahli, D. Sacchetto, N. Tétreault, B. Paviet-Salomon, S.-J. Moon, C. Allebé, M. Despeisse, S. Nicolay, S. D. Wolf, B. Niesen and C. Ballif, *ACS Energy Lett.*, 2016, **1**, 474-480.
34. J. Werner, C.-H. Weng, A. Walter, L. Fesquet, J. P. Seif, S. D. Wolf, B. Niesen and C. Ballif, *J. Phys. Chem. Lett.*, 2015, **7**, 161-166.
35. G. E. Eperon, T. Leijtens, K. A. Bush, R. Prasanna, T. Green, J. T.-W. Wang, D. P. McMeekin, G. Volonakis, R. L. Milot, R. May, A. Palmstrom, D. J. Slotcavage, R. A. Belisle, J. B. Patel, E. S. Parrott, R. J. Sutton, W. Ma, F. Moghadam, B. Conings, A. Babayigit, H.-G. Boyen, S. Bent, F. Giustino, L. M. Herz, M. B. Johnston, M. D. McGehee and H. J. Snaith, *Science*, 2016, DOI: 10.1126/science.aaf9717.
36. F. Fu, T. Feurer, T. Jäger, E. Avancini, B. Bissig, S. Yoon, S. Buecheler and A. N. Tiwari, *Nature Communications*, 2015, **6**, 8932.

37. Y. M. Yang, Q. Chen, Y.-T. Hsieh, T.-B. Song, N. D. Marco, H. Zhou and Y. Yang, *ACS Nano*, 2015, **9**, 7714-7721.
38. T. Todorov, T. Gershon, O. Gunawan, Y. S. Lee, C. Sturdevant, L. Y. Chang and S. Guha, *Adv. Energy Mater.*, 2015, **5**, 1500799.
39. A. R. Uhl, J. K. Katahara and H. W. Hillhouse, *Energy & Environmental Science*, 2016, **9**, 130-134.
40. Z. Yang, C.-C. Chueh, P.-W. Liang, M. Crump, F. Lin, Z. Zhu and A. K.-Y. Jen, *Nano Energy*, 2016, **22**, 328–337.
41. N. H. Reich, W. G. J. H. M. vanSark, E. A. Alsema, R. W. Lof, R. E. I. Schropp, W. C. Sinke and W. C. Turkenburg, *Sol. Energ. Mat. Sol. Cells*, 2009, **93**, 1471–1481.
42. A. Virtuani, E. Lotter and M. Powalla, *Thin Solid Films*, 2003, **431**, 443–447.
43. M. Gloeckler and J. R. Sites, *Thin Solid Films*, 2005, **480-481**, 241-245.
44. A. O. Pudov, A. Kanevce, H. A. Al-Thani, J. R. Sites and F. S. Hasoon, *J. Appl. Phys.*, 2005, **97**, 064901.
45. I. L. Eisgruber, J. E. Granata, J. R. Sites, J. Hou and J. Kessler, *Sol. Energ. Mat. Sol. Cells*, 1998, **53**, 367–377.
46. M. Turcu, I. M. Kötschau and U. Rau, *J. Appl. Phys.*, 2002, **91**, 1391.
47. R. Scheer and H.-W. Schock, *Chalcogenide Photovoltaics: Physics Technologies, and Thin Film Devices*, WILEY-VCH, Weinheim, Germany, 2011.
48. C.-C. Chueh, C.-Z. Li and A. K.-Y. Jen, *Energy Environ. Sci.*, 2015, **8**, 1160-1189.
49. J. Luo, J.-H. Im, M. T. Mayer, M. Schreier, M. K. Nazeeruddin, N.-G. Park, S. D. Tilley, H. J. Fan and M. Grätzel, *Science*, 2014, **345**, 1593-1596.
50. P. W. Liang, C. C. Chueh, X. K. Xin, F. Zuo, S. T. Williams, C. Y. Liao and A. K. Y. Jen, *Adv. Energy Mater.*, 2015, **5**, 1400960.
51. K. M. O'Malley, C. Z. Li, H. L. Yip and A. K. Y. Jen, *Adv. Energy Mater.*, 2011, **2**, 82-86.
52. D. Langley, G. Giusti, C. Mayousse, C. Celle, D. Bellet and J.-P. Simonato, *Nanotechnology*, 2013, **24**, 452001.
53. J. H. Kim, S. T. Williams, N. Cho, C. C. Chueh and A. K. Y. Jen, *Adv. Energy Mater.*, 2015, DOI: 10.1002/aenm.201401229.
54. J. W. Jung, C.-C. Chueh and A. K.-Y. Jen, *Advanced Materials*, 2015, **27**, 7874-7880.
55. M. Lee, S. J. Park, Y. J. Hwang, Y. Jun and B. K. Min, *Adv. Optical Mater.*, 2016, DOI: 10.1002/adom.201600373.
56. S. R. Kurtz, D. Myers and J. M. Olson, *26th IEEE PVSC*, 1997, 875-878.
57. S. Reynolds and V. Smirnov, *Energy Procedia*, 2015, **84**, 251-260.
58. Y. Liu, L. A. Renna, M. Bag, Z. A. Page, P. Kim, J. Choi, T. Emrick, D. Venkataraman and T. P. Russell, *ACS Appl. Mater. Interfaces*, 2016, **8**, 7070-7076.
59. S. Albrecht, M. Saliba, J. P. C. Baena, F. Lang, L. Kegelmann, M. Mews, L. Steier, A. Abate, J. Rappich, L. Korte, R. Schlatmann, M. K. Nazeeruddin, A. Hagfeldt, M. Grätzel and B. Rech, *Energy Environ. Sci.*, 2015, **9**, 81-88.